



HAL
open science

The Evolution and Role of Solar Wind Turbulence in the Inner Heliosphere

C. Chen, S. Bale, J. Bonnell, D. Borovikov, T. Bowen, D. Burgess, A. Case, B. Chandran, Thierry Dudok de Wit, K. Goetz, et al.

► **To cite this version:**

C. Chen, S. Bale, J. Bonnell, D. Borovikov, T. Bowen, et al.. The Evolution and Role of Solar Wind Turbulence in the Inner Heliosphere. The Astrophysical Journal Supplement, 2020, Early Results from Parker Solar Probe: Ushering a New Frontier in Space Exploration, 246 (2), pp.53. 10.3847/1538-4365/ab60a3 . insu-02937674

HAL Id: insu-02937674

<https://insu.hal.science/insu-02937674>

Submitted on 17 Sep 2020

HAL is a multi-disciplinary open access archive for the deposit and dissemination of scientific research documents, whether they are published or not. The documents may come from teaching and research institutions in France or abroad, or from public or private research centers.

L'archive ouverte pluridisciplinaire **HAL**, est destinée au dépôt et à la diffusion de documents scientifiques de niveau recherche, publiés ou non, émanant des établissements d'enseignement et de recherche français ou étrangers, des laboratoires publics ou privés.



Distributed under a Creative Commons Attribution - NoDerivatives 4.0 International License



The Evolution and Role of Solar Wind Turbulence in the Inner Heliosphere

C. H. K. Chen¹, S. D. Bale^{1,2,3,4}, J. W. Bonnell³, D. Borovikov⁵, T. A. Bowen³, D. Burgess¹, A. W. Case⁶, B. D. G. Chandran^{5,7}, T. Dudok de Wit⁸, K. Goetz⁹, P. R. Harvey³, J. C. Kasper^{6,10}, K. G. Klein¹¹, K. E. Korreck⁶, D. Larson³, R. Livi³, R. J. MacDowall¹², D. M. Malaspina¹³, A. Mallet³, M. D. McManus³, M. Moncuquet¹⁴, M. Pulupa³, M. L. Stevens⁶, and P. Whittlesey³

¹ School of Physics and Astronomy, Queen Mary University of London, London E1 4NS, UK; christopher.chen@qmul.ac.uk

² Physics Department, University of California, Berkeley, CA 94720-7300, USA

³ Space Sciences Laboratory, University of California, Berkeley, CA 94720-7450, USA

⁴ The Blackett Laboratory, Imperial College London, London, SW7 2AZ, UK

⁵ Space Science Center, University of New Hampshire, Durham, NH 03824, USA

⁶ Smithsonian Astrophysical Observatory, Cambridge, MA 02138 USA

⁷ Department of Physics & Astronomy, University of New Hampshire, Durham, NH 03824, USA

⁸ LPC2E, CNRS and University of Orléans, Orléans, France

⁹ School of Physics and Astronomy, University of Minnesota, Minneapolis, MN 55455, USA

¹⁰ Climate and Space Sciences and Engineering, University of Michigan, Ann Arbor, MI 48109, USA

¹¹ Lunar and Planetary Laboratory, University of Arizona, Tucson, AZ 85719, USA

¹² Solar System Exploration Division, NASA Goddard Space Flight Center, Greenbelt, MD 20771, USA

¹³ Laboratory for Atmospheric and Space Physics, University of Colorado, Boulder, CO 80303, USA

¹⁴ LESIA, Observatoire de Paris, Université PSL, CNRS, Sorbonne Université, Université de Paris, F-92195 Meudon, France

Received 2019 October 3; revised 2019 December 5; accepted 2019 December 9; published 2020 February 3

Abstract

The first two orbits of the *Parker Solar Probe* spacecraft have enabled the first in situ measurements of the solar wind down to a heliocentric distance of 0.17 au (or $36 R_{\odot}$). Here, we present an analysis of this data to study solar wind turbulence at 0.17 au and its evolution out to 1 au. While many features remain similar, key differences at 0.17 au include increased turbulence energy levels by more than an order of magnitude, a magnetic field spectral index of $-3/2$ matching that of the velocity and both Elsasser fields, a lower magnetic compressibility consistent with a smaller slow-mode kinetic energy fraction, and a much smaller outer scale that has had time for substantial nonlinear processing. There is also an overall increase in the dominance of outward-propagating Alfvénic fluctuations compared to inward-propagating ones, and the radial variation of the inward component is consistent with its generation by reflection from the large-scale gradient in Alfvén speed. The energy flux in this turbulence at 0.17 au was found to be $\sim 10\%$ of that in the bulk solar wind kinetic energy, becoming $\sim 40\%$ when extrapolated to the Alfvén point, and both the fraction and rate of increase of this flux toward the Sun are consistent with turbulence-driven models in which the solar wind is powered by this flux.

Unified Astronomy Thesaurus concepts: Solar wind (1534); Space plasmas (1544); Interplanetary turbulence (830); Interplanetary magnetic fields (824); Heliosphere (710); The Sun (1693); Alfvén waves (23); Plasma astrophysics (1261)

1. Introduction

The solar wind is observed to contain a turbulent cascade at distances from the closest previous in situ measurements to the Sun at 0.29 au (Tu & Marsch 1995) out to the edge of the heliosphere and beyond (Fraternali et al. 2019). Our understanding of solar wind turbulence and the role it plays in the large-scale dynamics, therefore, has come from measurements over this range of distances, much of which have been in the vicinity of 1 au (Alexandrova et al. 2013; Bruno & Carbone 2013; Kiyani et al. 2015; Chen 2016). The *Parker Solar Probe* (PSP) spacecraft (Fox et al. 2016) has so far traveled nearly twice as close to the Sun, down to a heliocentric distance of 0.17 au, and will get increasingly closer in future orbits. Measurements from PSP, therefore, are allowing this new environment to be used to investigate the fundamental nature of plasma turbulence and the role it plays in the generation of the solar wind.

At 1 au, it has long been known that the solar wind fluctuations at MHD scales are predominantly Alfvénic (Belcher & Davis 1971; Tu & Marsch 1995; Horbury et al. 2005; Bruno & Carbone 2013) with a small energy fraction in compressive fluctuations that resemble the slow mode (Tu & Marsch 1995; Howes et al. 2012; Klein et al. 2012; Bruno & Carbone 2013; Verscharen et al. 2017). The Alfvénic turbulence develops an anisotropic cascade that appears to be in critical balance (Horbury et al. 2008; Chen 2016), consistent with models of Alfvénic turbulence (Goldreich & Sridhar 1995; Boldyrev 2006; Lithwick et al. 2007; Beresnyak & Lazarian 2008; Perez & Boldyrev 2009; Chandran et al. 2015; Mallet & Schekochihin 2017). However, the different MHD fields typically display different scalings, which depend on underlying parameters, such as the level of imbalance between the oppositely directed Alfvénic fluxes, in a way that is not currently captured by any single model (Chen 2016). The compressive fluctuations are also highly anisotropic (Chen et al. 2012; Chen 2016) and thought to be passive with respect to the Alfvénic turbulence (Schekochihin et al. 2009).

Previous missions, such as *Helios*, *Voyager*, *Ulysses*, and the *Mariner* spacecraft have allowed the radial evolution of the

turbulence to be studied beyond 0.29 au. Some key findings from this data have been decreasing power levels with increasing distance (Belcher & Burchsted 1974; Villante 1980; Bavassano et al. 1982; Tu & Marsch 1995; Horbury & Balogh 2001), a “ $1/f$ ” break scale that moves to larger scales at greater distances (Bavassano et al. 1982; Horbury et al. 1996; Bruno & Carbone 2013), a correlation length that increases with distance (Tu & Marsch 1995; Ruiz et al. 2014), a reduction of the imbalance or cross-helicity with distance (Roberts et al. 1987; Tu & Marsch 1995; Bavassano et al. 1998, 2000; Matthaeus et al. 2004; Breech et al. 2005), and a velocity spectral index that evolves from $-3/2$ to $-5/3$ between 1 and 5 au (Roberts 2010). The evolution of all of these features is consistent with an active cascade occurring throughout the solar wind, which is also consistent with the observed nonadiabatic temperature profile suggesting continual heating of the plasma (Mihalov & Wolfe 1978; Gazis & Lazarus 1982; Marsch et al. 1982; Freeman 1988; Richardson et al. 1995; Matthaeus et al. 1999b; Cranmer et al. 2009; Hellinger et al. 2011).

In addition to this heating far from the Sun, turbulence is also proposed to play a key role in the heating of the solar corona and acceleration of the solar wind itself. Early solar wind models, based on the seminal work of Parker (1958), were based on a thermally driven wind, but it was quickly realized that this was not sufficient to lead to the observed solar wind properties 1 au (see reviews by Parker 1965; Leer et al. 1982; Barnes 1992; Hollweg 2008; Hansteen & Velli 2012; Cranmer et al. 2015). The propagation of Alfvén waves from the photosphere into the corona to drive a turbulent cascade was proposed as a possible solution; the waves and turbulence provide a pressure to directly accelerate the solar wind (Alazraki & Couturier 1971; Belcher 1971), and the dissipation of the turbulence can provide additional heating (Coleman 1968). The generation of this turbulence requires counterpropagating waves (Iroshnikov 1963; Kraichnan 1965), and the large-scale gradient in Alfvén speed was suggested to cause the outward-propagating waves to be partially reflected (Heinemann & Olbert 1980; Velli 1993) and initiate the cascade (Matthaeus et al. 1999a; Dmitruk et al. 2002; Cranmer & van Ballegoijen 2005; Verdini & Velli 2007; Chandran & Hollweg 2009; Verdini et al. 2009). Modern turbulence-driven models now incorporate these components, together with other properties such as heat fluxes, pressure anisotropy, and turbulent dissipation, to achieve self-consistent solar wind solutions that can match many properties of observational data (Cranmer et al. 2007; Verdini et al. 2010; Chandran et al. 2011; van der Holst et al. 2014; Usmanov et al. 2018). However, the key test for these and other classes of solar wind models are measurements close to the Sun where the heating and acceleration are taking place.

In this paper, data from *PSP* during its first two orbits are used to study turbulence down to a distance of 0.17 au from the Sun for the first time. The basic properties of the turbulence are investigated, along with its radial evolution out to ~ 1 au, and compared to models of MHD turbulence and models of Alfvénic turbulence-driven solar wind, to determine the properties, evolution, and role of solar wind turbulence in the inner heliosphere.

2. Data

The data used in this study, from the first two orbits of *PSP* from 2018 October 6th to 2019 April 18th, cover a heliocentric

radial distance range 0.17–0.82 au (or equivalently 35.7 to 174 R_{\odot}). From the *FIELDS* instrument suite (Bale et al. 2016), magnetic field data, \mathbf{B} , from the outboard fluxgate magnetometer (MAG) averaged to 0.4369 s resolution, and electron density, n_e , derived from quasi-thermal noise (QTN) measurements made by the Radio Frequency Spectrometer Low Frequency Receiver (RFS/LFR) at 6.991 s resolution (Moncuquet et al. 2020), were used. From the *SWEAP* instrument suite (Kasper et al. 2016), moments of the ion (proton) distributions (density n , velocity v , and radial temperature T_r) measured by the Solar Probe Cup (SPC) averaged to 27.96 s resolution over the full orbit, and at a resolution of 0.8738 s for a 1 day period during Perihelion 1, were used. In addition to the automated SPC data processing (Case et al. 2020), remaining unphysical data points were manually removed. Because the QTN density is more accurate closer to the Sun, a combination of QTN and SPC density was used: for each interval studied, the mean QTN density was used unless the density was not possible to calculate for more than half of the interval, in which case the average SPC density was used. This interval-averaged density was used to calculate the Alfvénic normalization, plasma beta, and energy fluxes for the analysis in this paper.

The solar wind over the two orbits was mostly slow wind, Alfvénic in nature, with large-amplitude ($\delta B/B \sim 1$) fluctuations (Bale et al. 2019; Kasper et al. 2020). The orbits covered a mixture of source regions, although notably much of the first encounter was in wind from a small low-latitude coronal hole (Bale et al. 2019; Badman et al. 2020). The ratio of the solar wind speed to Alfvén speed, v/v_A , was always larger than 1 throughout both orbits, and larger than 3 the majority of the time, indicating the Taylor (1938) hypothesis to be marginally well satisfied, which would enable temporal structure to be interpreted as spatial structure, i.e., spacecraft-frame frequencies f_{sc} to be interpreted as wavenumbers k through $k = (2\pi f_{sc})/v$. However, even in those parts of the orbit where $v/v_A \sim 1$, it has been shown that the Taylor hypothesis can hold for the dominant outward-propagating component of highly imbalanced (i.e., high cross-helicity) turbulence (Klein et al. 2015), and that when the Taylor hypothesis breaks down, the sweeping by larger-scale eddies leads to the same spectral index in the spacecraft-frame frequency spectra as the underlying wavenumber spectra (Bourouaine & Perez 2018, 2019). In this paper, the results are interpreted spatially.

3. Results

3.1. Turbulence Spectrum

To examine the radial evolution of the magnetic field fluctuation spectrum, the MAG data were divided into one-day intervals for analysis. Periods containing coronal mass ejections were removed, all data gaps were linearly interpolated, and days with more than 1% of the data missing were excluded from the analysis. For each interval, the trace power spectral density was calculated by Fourier transform and, for clarity, smoothed by averaging over a sliding window of a factor of 2. The power spectra, E_B , as a function of spacecraft-frame frequency f_{sc} , are shown in Figure 1, in which they are colored by heliocentric distance, r . It can be seen that the power levels systematically increase as r decreases by at least two orders of magnitude over the range considered. For frequencies $10^{-3} \text{ Hz} \lesssim f_{sc} \lesssim 10^{-1} \text{ Hz}$, a power-law range that is compatible with models of inertial range MHD turbulence (discussed below) is present at all

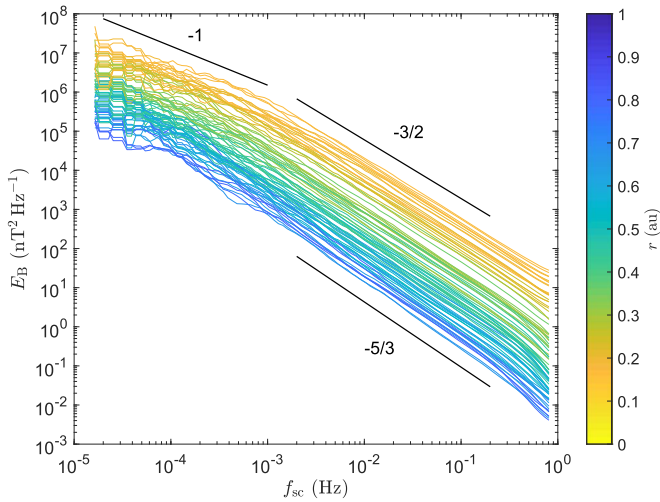


Figure 1. Magnetic field power spectrum, E_B , at different heliocentric distances, r , over the first two *PSP* orbits. Several power-law slopes are marked for comparison. A turbulent inertial range is present at all distances, with a flattening at low frequencies. Deviations at high frequencies ($f_{sc} \gtrsim 0.3$ Hz) are partly due to digital filter effects.

distances, and at lower frequencies, a flattening, here compared to f_{sc}^{-1} , is present (although this low-frequency range is not the focus of the present study). Typical ion kinetic scales are at $f_{sc} \gtrsim 1$ Hz (Duan et al. 2020) so that all of the analysis in this paper corresponds to the MHD inertial range.

A key diagnostic of the turbulence used to distinguish the nature of the cascade process is the power-law spectral index α , defined through $E \propto f_{sc}^\alpha$. This was calculated for each magnetic spectrum in the frequency range 10^{-2} Hz $< f_{sc} < 10^{-1}$ Hz and is shown as a function of radial distance in Figure 2. A clear transition can be seen from $\alpha_B \approx -3/2$ at $r \approx 0.17$ au to $\alpha_B \approx -5/3$ at $r \approx 0.6$ au. This variation is consistent across all phases of the first two *PSP* orbits and has not been observed before, as in situ measurements have previously only been available for $r \gtrsim 0.3$ au where the transition occurs. It can be seen that there is some scatter in the data; this may be in part due to statistical variation but could also be due to varying solar wind conditions and underlying parameters that control magnetic spectrum.

Figure 3 shows the trace spectra of the Alfvénic turbulence variables for the 24 hr period of the day of Perihelion 1, 2018 November 6th, at 0.17 au. The spectra are of the magnetic field in Alfvén units, $\mathbf{b} = \mathbf{B}/\sqrt{\mu_0 \rho_0}$, where ρ_0 is the average mass density, the velocity \mathbf{v} , the Elsasser (1950) variables, $\mathbf{z}^\pm = \mathbf{v} \pm \mathbf{b}$, describing the inward- and outward-propagating Alfvénic fluctuations, and the total energy $E_t = E_b + E_v = E_+ + E_-$ (note that the Elsasser spectra are defined with an additional factor of $\frac{1}{2}$ such that they sum to the total energy spectrum). It can be seen that all fields take a spectral index close to $\alpha \approx -3/2$ in the inertial range $f_{sc} \gtrsim 2 \times 10^{-3}$ Hz, until some (in particular E_- and E_v) show an artificial flattening at high frequencies, due to velocity noise.¹⁵ This results in an approximately constant Alfvén ratio, $r_A = E_v/E_b$, and Elsasser ratio, $r_E = E_+/E_-$, through the measured inertial range ($2 \times 10^{-3} \lesssim f_{sc} \lesssim 5 \times 10^{-2}$ Hz).¹⁶

¹⁵ The $-3/2$ velocity spectrum extends down to the ion kinetic scales during the short periods when SPC was operating in flux angle mode, which has a lower noise level (Vech et al. 2020).

¹⁶ Note, however, that Parashar et al. (2020) report times in which the level of imbalance appears not to be constant through the inertial range.

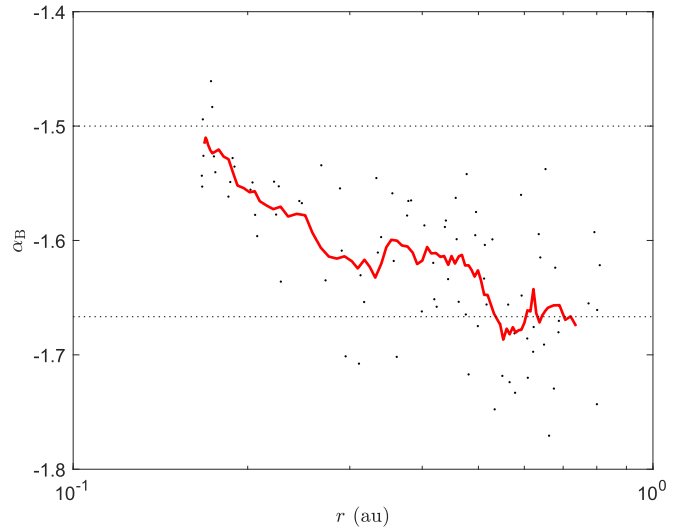


Figure 2. Variation of the magnetic field spectral index, α_B , with heliocentric distance, r , in the MHD inertial range (10^{-2} Hz $< f_{sc} < 10^{-1}$ Hz). The black dots show the spectral index measurements, and the red line is a 10-point running mean. The horizontal dotted lines mark the theoretical predictions $-3/2$ and $-5/3$.

The average values, calculated as the mean of all of the values within this range, are $r_A = 0.69$ and $r_E = 14.6$, indicating highly imbalanced outward-dominated Alfvénic turbulence with a small amount of residual energy.¹⁷

One possibility for the radial variation of the magnetic spectral index (Figure 2) is that the shallower spectrum near the Sun reflects a transient stage of evolution, similar to the suggestion by Roberts (2010) for the steepening of the velocity spectrum reported for $r > 1$ au. However, even by 0.17 au, there have been a large number of nonlinear times (see Section 3.5), meaning that the inertial range should already be in steady state by this distance. Another possibility is that the spectral index depends on an underlying parameter, such as the normalized cross-helicity $\sigma_c = 2\langle \delta \mathbf{b} \cdot \delta \mathbf{v} \rangle / \langle \delta \mathbf{b}^2 + \delta \mathbf{v}^2 \rangle$ or normalized residual energy $\sigma_r = 2\langle \delta \mathbf{z}^+ \cdot \delta \mathbf{z}^- \rangle / \langle \delta \mathbf{z}^{+2} + \delta \mathbf{z}^{-2} \rangle$. Measurements at 1 au (Podesta & Borovsky 2010; Chen et al. 2013; Wicks et al. 2013; Bowen et al. 2018b) have shown that α_B depends on both of these quantities, taking a value of $\approx -3/2$ when $|\sigma_c| \approx 1$ or $|\sigma_r| \approx 0$ and steeper otherwise. To test this, the radial variation of σ_c and σ_r was calculated from 6 hr averages (with intervals containing heliospheric current sheet crossings removed; Szabo et al. 2020), and the results are shown in Figure 4. The direction of \mathbf{B} was “rectified” (Bruno et al. 1985; Roberts et al. 1987) with respect to the average sign of B_r over the interval so that \mathbf{z}^+ corresponds to outward-propagating Alfvénic fluctuations and \mathbf{z}^- to the inward-propagating ones. There is significant scatter, which reflects the varying solar wind conditions, but it can be seen that on average σ_c decreases with increasing r (from ≈ 0.8 to ≈ 0.3) and σ_r is roughly constant at ≈ -0.2 .¹⁸ Therefore, the measurements are consistent with the previous dependence of α_B on σ_c at 1 au, although this does not seem to be related to a change in residual energy.

¹⁷ Pressure anisotropy can sometimes lead to significant modifications of the Alfvén ratio (Chen et al. 2013), although these were not found to be important here due to the low β .

¹⁸ See McManus et al. (2020) for details of the local properties of σ_c and σ_r measured by *PSP* at perihelion.

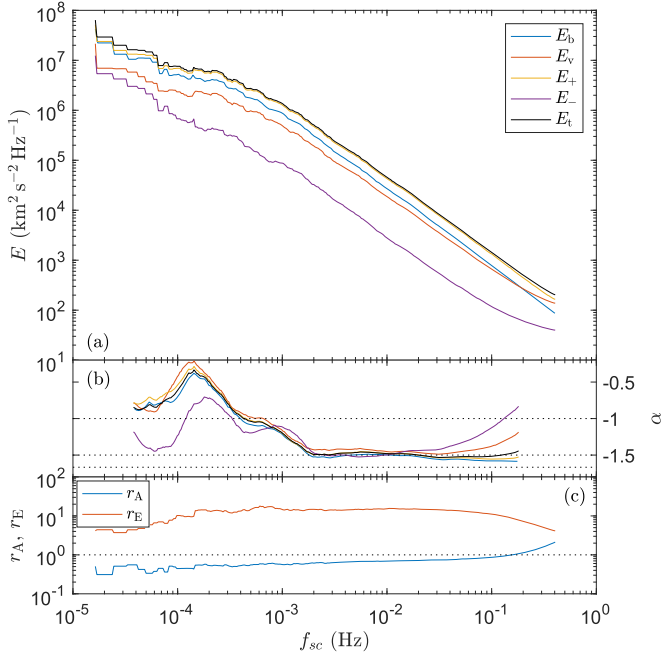


Figure 3. (a) Spectra of Alfvénic turbulence variables at 0.17 au. (b) Local spectral index α (calculated over a sliding window of a factor of 5), together with dotted lines marking values -1 , $-3/2$, and $-5/3$. (c) Alfvén ratio, r_A , and Elsasser ratio, r_E .

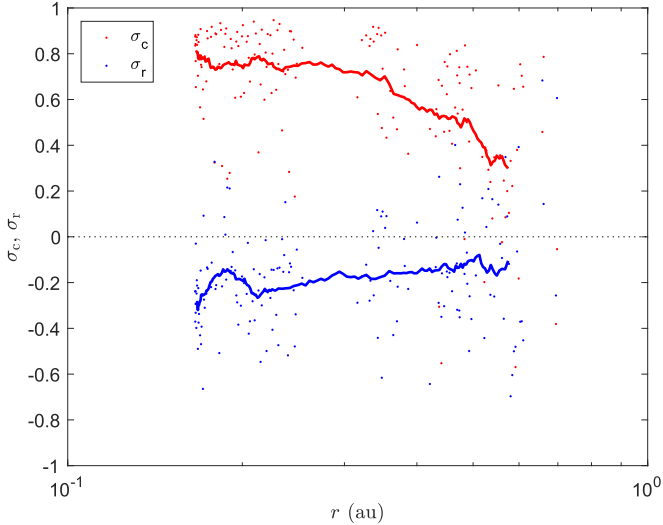


Figure 4. Dependence of normalized cross-helicity, σ_c , and residual energy, σ_r , on heliocentric distance r . The dots mark 6 hr average values, and the solid lines are 30-point running means.

Regarding the cause of the $-3/2$ spectra at 0.17 au, this scaling is consistent¹⁹ with models of both balanced (Boldyrev 2006; Chandran et al. 2015; Mallet & Schekochihin 2017) and imbalanced (Perez & Boldyrev 2009; Podesta & Bhattacharjee 2010) Alfvénic turbulence in homogeneous plasmas (e.g., without wave reflection) that involve scale-dependent alignment. In addition, recent simulations (Chandran & Perez 2019) of inhomogeneous reflection-driven MHD turbulence from the photosphere to $21 R_\odot$ found that both E_+ and E_- also tend

¹⁹ Because the local mean field is not being tracked, the measured frequency spectra can be interpreted as k_\perp spectra, assuming $k_\perp \gg k_\parallel$ (as expected theoretically and measured at 1 au; e.g., Chen 2016).

toward $\alpha = -3/2$ past the Alfvén point for a range of values of the correlation time and perpendicular correlation length at the photosphere. Chandran & Perez (2019) considered this in partial agreement with a reflection-driven version of the Lithwick et al. (2007) model of strong imbalanced MHD turbulence, which predicts the same spectral index ($\alpha = -5/3$) for both E_+ and E_- , with the $-3/2$ scaling possibly resulting from additional phenomena such as intermittency and scale-dependent alignment (e.g., Boldyrev 2006; Chandran et al. 2015). However, it is also possible that the trend seen in Figure 2 is partway through a transition from an even shallower spectrum closer to the Sun or an effect of the driving on the cascade; these possibilities are discussed further in Section 4.

3.2. Magnetic Compressibility and Slow-mode Fraction

Another well-known feature of solar wind turbulence is the low power in compressive fluctuations, in particular the low level of fluctuations in $|\mathbf{B}|$ (e.g., Bruno & Carbone 2013; Chen 2016). Figure 5(a) shows the magnetic compressibility, $C_B = (\delta|\mathbf{B}|/|\delta\mathbf{B}|)^2$, as a function of r at four spacecraft-frame frequencies. C_B decreases toward smaller r at all frequencies, which is independent of f_{sc} through the inertial range ($f_{sc} \gtrsim 10^{-3}$ Hz). Overall, the compressibility levels at perihelion are an order of magnitude smaller than at 1 au. Figure 5(b) shows the compressibility as a function of r at $f_{sc} = 10^{-2}$ Hz, colored by solar wind speed. It can be seen that the periods of faster wind $v \gtrsim 500$ km s⁻¹ (observed by PSP on the outbound part of its first orbit between 0.3 and 0.5 au) have a lower compressibility, consistent with previous observations at larger r (Tu & Marsch 1995; Bruno & Carbone 2013), and overall, the data can be fit to a power law, $C_B \propto r^{1.68 \pm 0.23}$, although with significant scatter.

Measurements at 1 au (Howes et al. 2012; Klein et al. 2012; Verscharen et al. 2017), as well as an analysis of PSP data (Chaston et al. 2020), suggest that the compressive power is primarily in slow-mode-like fluctuations, so it is of interest to see if the radial variation in compressibility is due to varying β or varying slow-mode fraction. If it is assumed that δB_\perp arises from the Alfvén mode and $\delta|\mathbf{B}| \approx \delta B_\parallel$ from the slow mode, the compressibility is given by²⁰

$$C_B = \frac{\epsilon^2 \beta \gamma \sin^4(\theta_{kB})}{2}, \quad (1)$$

where γ is the adiabatic index, $\epsilon = \delta v_{\parallel,s}/\delta v_{\perp,A}$ is the ratio of slow to Alfvén wave amplitudes, and θ_{kB} is the slow-wave propagation angle. The dependence of C_B on β is shown in Figure 5(c), where it is indeed seen to be linear to within errors of the fit, consistent with Equation (1). There is, however, also much scatter, which may be a result of variation in the other parameters. The slow-mode kinetic energy fraction, ϵ^2 , can be estimated directly from Equation (1), assuming $\gamma = 5/3$ and $\sin(\theta_{kB}) = 1$.²¹ The result, as a function of r , is shown in Figure 5(d), in which it can be seen that ϵ^2 varies with distance to the Sun as $\epsilon^2 \propto r^{1.18 \pm 0.19}$. This indicates that the lower magnetic compressibility seen by PSP near perihelion is not

²⁰ While this is derived from MHD, which is not in principle applicable to the solar wind due to its low collisionality, recent measurements suggest the slow-mode fluctuations to be fluid-like in their polarizations (Verscharen et al. 2017), suggesting Equation (1) may be a reasonable approximation.

²¹ Measurements show that the compressive fluctuations are highly anisotropic at 1 au (Chen et al. 2012; Chen 2016) so that $\sin(\theta_{kB}) \approx 1$.

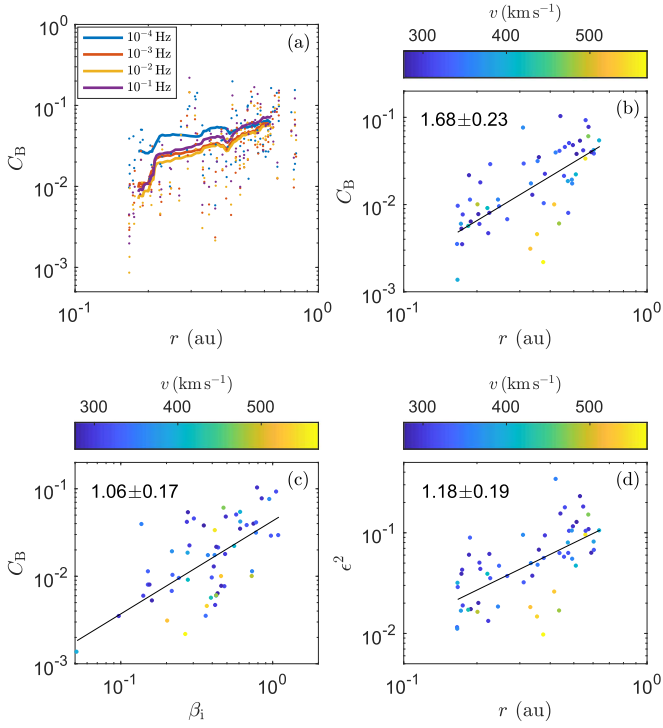


Figure 5. (a) Magnetic compressibility, C_B , as a function of heliocentric distance, r , at four values of spacecraft-frame frequency f_{sc} : the solid lines are 30-point running means. (b) C_B as a function of r at $f_{sc} = 10^{-2}$ Hz colored by solar wind speed, v . (c) C_B as a function of ion plasma beta, β_i . (d) Slow-mode kinetic energy fraction, ϵ^2 , as a function of r .

just due to the lower β but also a reduced slow-mode component, and that there is an additional process acting to increase this compressive component of the solar wind as it travels away from the Sun.

3.3. Energy Flux and Solar Wind Acceleration

To determine the role that turbulence plays in the generation of the solar wind, a key measurement is the energy flux of the fluctuations near the Sun. The two dominant contributions to the energy flux in wave- and turbulence-driven solar wind models (e.g., Belcher 1971; Alazraki & Couturier 1971; Chandran et al. 2011) are the enthalpy flux of the outward-propagating Alfvénic fluctuations,

$$F_A = \frac{\rho |\delta z^+|^2}{4} \left(\frac{3}{2} v_r + v_A \right), \quad (2)$$

and the bulk flow kinetic energy flux of the solar wind,

$$F_k = \frac{1}{2} \rho v_r^3, \quad (3)$$

where v_r is the radial component of the solar wind velocity. The ratio of these two terms, calculated from 6 hr rms values of δz^+ to capture the full extent of the inertial range and outer scale, is shown as a function of r in Figure 6(a). It can be seen that this ratio increases as r decreases and over this range of distances can be fit by a power law, $F_A/F_k \propto r^{-1.75 \pm 0.10}$. At 0.17 au, this ratio is ~ 20 times larger than at 1 au, with a value of $\sim 10\%$. The Alfvénic flux itself (not shown) also varies as a power law, $F_A \propto r^{-3.52 \pm 0.12}$, taking a value $F_A = 0.72 \text{ mW m}^{-2}$ at 0.17 au. The same ratio, plotted as a function of radial Alfvén

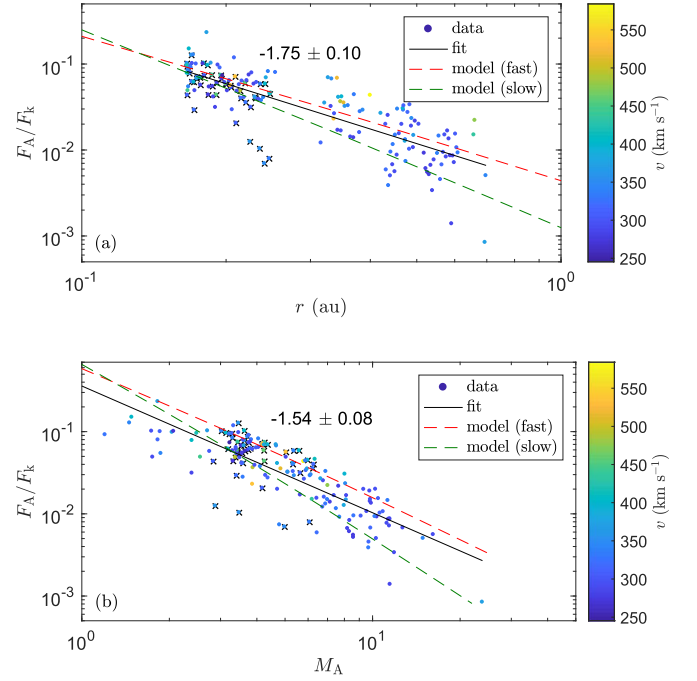


Figure 6. (a) Ratio of outward-propagating Alfvénic energy flux, F_A , to solar wind bulk kinetic energy flux, F_k , as a function of heliocentric distance, r . (b) The same ratio as a function of solar wind radial Alfvén Mach number, M_A . In both plots, the black solid line is a power-law fit, the red/green dashed lines are the fast/slow solar wind model solutions described in the text, the data points are colored by solar wind speed, v , and crosses mark times during connection to the coronal hole in Encounter 1.

Mach number, $M_A = v_r/v_A$, is shown in Figure 6(b), where it can be seen to take a dependence $F_A/F_k \propto M_A^{-1.54 \pm 0.08}$. Extrapolating this to the Alfvén point ($M_A = 1$) gives a ratio of $\sim 40\%$, indicating that within the corona there is likely to be a significant fraction of the solar wind energy flux in Alfvénic turbulence.

Also plotted in Figure 6 are the flux ratios from two solutions of the solar wind model of Chandran et al. (2011). The model describes a solar wind driven primarily by Alfvénic turbulence (that provides both heating and wave pressure), but also contains collisional and collisionless heat fluxes. The solutions are for a fast wind (800 km s^{-1} at 1 au) as described in Chandran et al. (2011) and a slow wind (337 km s^{-1} at 1 au) chosen to match bulk solar wind values measured during Encounter 1, and the model parameters are given in Table 1. It can be seen that there is a reasonable match between both the fast and slow wind solutions and the measurements, both in terms of the absolute level and approximate power-law trends, indicating that these observations are consistent with such a turbulence-driven solar wind. One consideration is that the observations are for slow solar wind: in Figure 6, all data are for $v < 600 \text{ km s}^{-1}$. However, near perihelion, much of this was Alfvénic slow wind, in particular from the equatorial coronal hole during Encounter 1 (Bale et al. 2019; Badman et al. 2020), to which the wave- and turbulence-driven models are thought to provide a good description (Cranmer et al. 2007). Times during connection to this coronal hole are marked with crosses in Figure 6; most of these points lie close to the model solutions, although there are a few significantly below. These correspond to intervals containing quiet radial-field wind during which the turbulent amplitudes are much lower (Bale et al. 2019).

Table 1

Parameters Used in the Fast and Slow Wind Model Solutions in Figure 6

Parameter	Fast	Slow
B_{\odot}	11.8 G	10.2 G
n_{\odot}	10^8 cm^{-3}	$4 \times 10^8 \text{ cm}^{-3}$
T_{\odot}	$7 \times 10^5 \text{ K}$	$8.79 \times 10^5 \text{ K}$
δv_{\odot}	41.4 km s^{-1}	27.6 km s^{-1}
f_{max}	9	8
R_1	$1.29 R_{\odot}$	$0.3 R_{\odot}$
$L_{\perp\odot}$	10^3 km	10^3 km
c_d	0.75	1.35
c_2	0.17	0.17
α_H	0.75	0.75
r_H	$5 R_{\odot}$	$30 R_{\odot}$

Note. See Chandran et al. (2011) for parameter definitions.

3.4. Power Levels and Inward Fluctuations

It is also of interest to determine the radial variation of the inward-propagating fluctuations to provide information about their origin. Inward-propagating modes are necessary for any nonlinear Alfvénic interaction, but any generated inside the Alfvén point would not travel farther out (because $v < v_A$), meaning that those observed beyond the Alfvén point must be generated locally. Figure 7 shows the variation of the Elsasser energies calculated over 6 hr intervals as a function of r . It can be seen that the inward-propagating fluctuations have a much shallower radial variation than the outward-propagating ones, similar to previous measurements between 0.4 and 3 au (Bavassano et al. 2000), and qualitatively consistent with predictions from turbulent evolution models (e.g., Verdini & Velli 2007; Chandran & Hollweg 2009). The power-law variations measured here are $|\delta z^-|^2 \propto r^{-0.51 \pm 0.11}$ and $|\delta z^+|^2 \propto r^{-1.72 \pm 0.12}$.

While several processes may generate inward-propagating fluctuations beyond the Alfvén point (see, e.g., Bruno 2006), reflection due to the large-scale gradient in v_A is thought to be a key mechanism for this, especially at smaller r (Heinemann & Olbert 1980; Dmitruk et al. 2002; Chandran & Hollweg 2009; Chandran et al. 2011; Perez & Chandran 2013; Chandran & Perez 2019). In the model of Chandran et al. (2011), the inward-propagating fluctuation amplitude is given by

$$\delta z^- = L_{\perp\odot} \sqrt{\frac{B_{\odot}}{B}} \left(\frac{v_r + v_A}{v_A} \right) \left| \frac{\partial v_A}{\partial r} \right|, \quad (4)$$

which describes a balance between its generation by reflection and dissipation through the turbulent cascade. By fitting the measured v_A to a power law in r , taking the gradient of the fit, and calculating the right-hand-side of Equation (4) for each data point, the predicted radial variation of $|\delta z^-|^2$ was determined. The power-law fit to the predicted amplitudes, taking $L_{\perp\odot} = 1.4 \times 10^4 \text{ km}$ as the correlation length and $B_{\odot} = 1.18 \text{ mT}$ as the magnetic field at the base of the corona, is marked in Figure 7 as the green line and has a variation $\propto r^{-0.58}$. This power law is a good match to that observed, and the values of $L_{\perp\odot}$ and B_{\odot} are within a reasonable expected range (Chandran et al. 2011; Chandran & Perez 2019), indicating that the inward-propagating fluctuations are consistent with being generated by reflection past the Alfvén point. However, it remains possible that other mechanisms such as

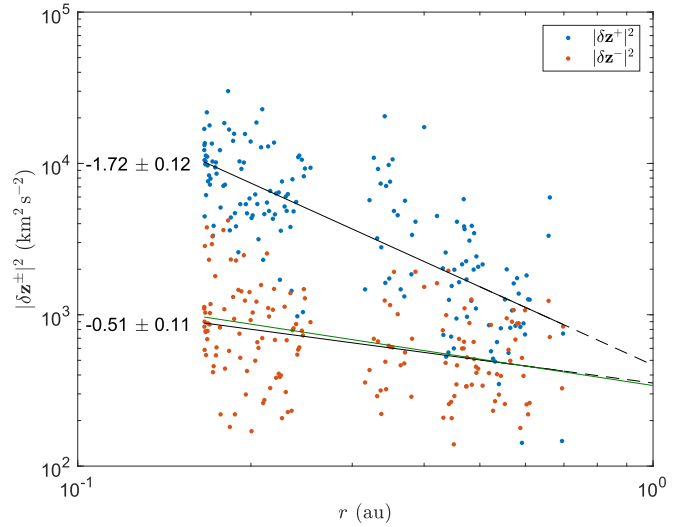


Figure 7. Energy in Elsasser fluctuations as a function of heliocentric distance, r , with power-law fits marked as solid lines. The green line is the predicted $|\delta z^-|^2$ evolution from Equation (4).

local driving or parametric decay may also contribute, and further analysis will be needed to test these.

3.5. Turbulence Outer Scale

Finally, the evolution of the outer scale of the turbulence was examined. The outer scale can be defined observationally in several ways, e.g., as the beginning of the MHD turbulence scaling range or as the correlation length of the fluctuations. Second-order structure functions of the magnetic field,

$$\delta \mathbf{B}^2(\tau) = \langle |\mathbf{B}(t + \tau) - \mathbf{B}(t)|^2 \rangle, \quad (5)$$

can be used to define the scaling ranges and are shown in Figure 8(a) calculated at different r over one-day intervals. It can be seen that they have a steeper scaling at smaller scales and a flat range at larger scales, consistent with the spectra in Figure 1.²² At each distance, a power-law fit was made in the inertial range (10–100 s) and the value at large scales was determined by an average of the points with $\tau > 10^4 \text{ s}$; the break scale, τ_b , was determined as the point at which these two lines cross (example fits are shown in Figure 8(a) for the highest and lowest amplitude curves). Figure 8(b) shows the normalized magnetic field correlation functions,

$$C(\tau) = \frac{\langle \delta \mathbf{B}(t + \tau) \cdot \delta \mathbf{B}(t) \rangle}{\langle |\delta \mathbf{B}|^2 \rangle}, \quad (6)$$

where $\delta \mathbf{B}(t) = \mathbf{B}(t) - \langle \mathbf{B} \rangle$, also for one-day intervals.²³ The correlation scale, τ_c , can be obtained from $C(\tau)$ in various ways (e.g., Ruiz et al. 2014; Isaacs et al. 2015); here, it was taken as the point where C decreases such that $C(\tau_c) = e^{-1}$.

The radial variation of the two outer-scale estimates, τ_b and τ_c , is shown in Figures 9(a) and (b). For both quantities, there is

²² A flat structure function corresponds to a spectrum with spectral index -1 or shallower (Monin & Yaglom 1975).

²³ While the solar wind correlation time has been shown to depend on the length of the interval used to calculate it (Matthaeus & Goldstein 1982; Isaacs et al. 2015; Krishna Jagarlamudi et al. 2019), here we choose one-day intervals as a reasonable compromise and are more interested in its radial dependence than absolute value.

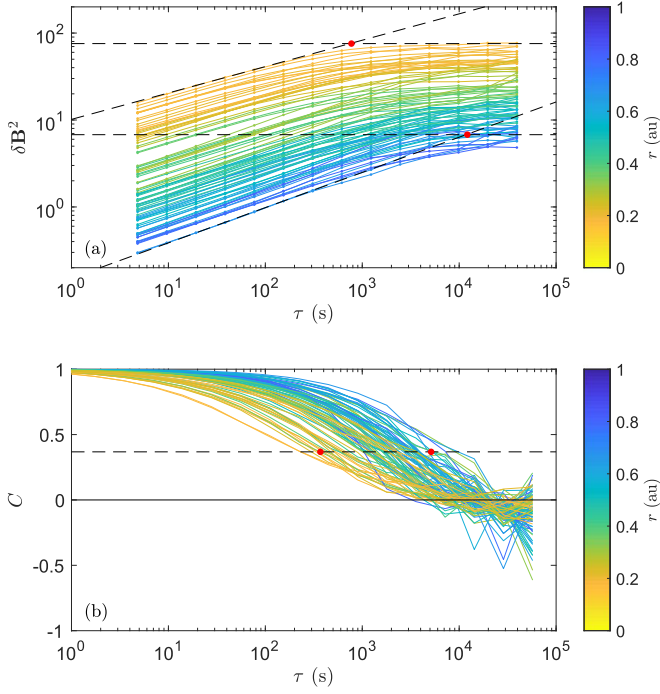


Figure 8. (a) Second-order structure function, δB^2 , at different heliocentric distances, r , with two examples of power-law fits (black dashed) determining the break scale (red dots). (b) Magnetic field correlation function, C , at different r showing the correlation time (red dots) at $C = e^{-1}$ (black dashed) for the same two examples.

a loose positive correlation and an increase of the outer scale with distance as $\tau_{b,c} \propto r^{1.1}$, although there is substantial scatter in the data. Figure 9(c) shows that there is a good correspondence between τ_b and τ_c , which is consistent with the structure function and correlation function being directly related quantities (Monin & Yaglom 1975). It can be seen that much of the scatter in Figures 9(a) and (b) can be attributed to the variation in solar wind speed: faster wind has an outer scale at smaller scales. This can be in part because the Taylor shift in faster wind results in the same k appearing at a smaller τ , but can also be due to a physical difference, such as slower wind having a larger travel time and therefore a break scale at larger τ if it is set by the scale at which the largest eddies have had time to decay (Matthaeus & Goldstein 1986). Figure 9(d) shows the Taylor-shifted break wavenumber, $k_b = 2\pi/(\tau_b v)$, as a function of the travel time from the Sun (assuming constant solar wind speed), $T = r/v$, where a better correlation can be seen, and the solar wind speed dependence is no longer present.

Figures 9(e) and (f) show the nonlinear time at the outer scale, defined²⁴ from the velocity fluctuations as $\tau_{nl}^v = (k_b \delta v_{rms})^{-1}$ and from the δz^- fluctuations (i.e., the timescale for the δz^+ fluctuations) as $\tau_{nl}^+ = (k_b \delta z_{rms}^-)^{-1}$, as a function of T . It can be

²⁴ Equating τ_{nl}^+ and $(k_b \delta z_{rms}^-)^{-1}$ follows from models of inhomogeneous reflection-driven solar wind turbulence, in which the z^+ fluctuations continually interact with their own reflections and the reflections of the z^+ fluctuations just “ahead” of them, i.e., at larger r (e.g., Velli et al. 1989; van Ballegoijen & Asgari-Targhi 2017). Note, however, that in some models of imbalanced MHD turbulence without wave reflections, τ_{nl}^+ can be much larger than $(k_b \delta z_{rms}^-)^{-1}$ (e.g., Beresnyak & Lazarian 2008), in which case the nonlinear time for z^+ would be significantly longer than measured here. Also, these definitions do not include the alignment angle between δz^+ and δz^- , but because the turbulence here is significantly imbalanced with only a small residual energy, this angle is large and the correction is of order unity.

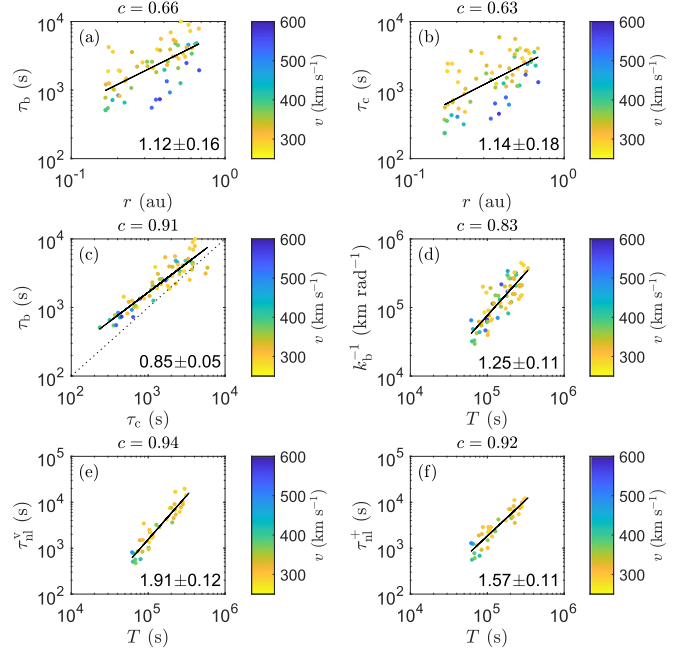


Figure 9. (a) Break scale, τ_b , as a function of heliocentric distance, r . (b) Correlation scale, τ_c , as a function of r . (c) Comparison between the two outer scales. (d) τ_b as a function of travel time from the Sun, T . (e) Break-scale velocity nonlinear time τ_{nl}^v as a function of T . (f) Break-scale Elsasser nonlinear time τ_{nl}^+ as a function of T . For each panel, the correlation coefficient c is given.

Table 2

Measured Correlation Times for the Different MHD Turbulence Fields

Field	τ_c
B	417 s
v	419 s
z^+	407 s
z^-	3300 s

seen that in both cases there is a good correlation, but the power-law dependence is much stronger than linear and $\tau_{nl}^v, \tau_{nl}^+ \ll T$. This indicates that the fluctuations in the large-scale flat scaling range have had significant time for nonlinear processing, and increasingly so closer to the Sun. This would suggest that this range might not be a simple spectrum of non-interacting waves, but could be undergoing nonlinear interactions, as in more recent models of the $1/f$ range (Velli et al. 1989; Verdini et al. 2012; Perez & Chandran 2013; Chandran 2018; Matteini et al. 2018).

Finally, it is of interest to compare the correlation times of the different Alfvénic turbulence fields, which are shown in Table 2 for the day of Perihelion 1, 2018 November 6th. The magnetic, velocity, and outward Elsasser fields have correlation times of $\tau_c \sim 7$ minutes, whereas the inward Elsasser field has a correlation time eight times longer. All correlation times are shorter than those seen at 0.3 au by *Helios* (Tu & Marsch 1995, Table 1), consistent with the radial trend in τ_c described above. In addition, the ratio between the z^- and z^+ correlation times is greater than that seen by *Helios* at 0.3 au. The observation that z^- has a longer spacecraft-frame correlation time than z^+ is consistent with models in which the reflection of z^+ fluctuations is the source of the z^- fluctuations. Because the

z^+ fluctuations reflect more efficiently at lower frequencies (Heinemann & Olbert 1980; Velli 1993), the energy-weighted average frequency of the z^- fluctuations is smaller than that of the z^+ fluctuations, which implies that the characteristic correlation length of the z^- fluctuations is larger than that of the z^+ fluctuations. Therefore, the observed difference in correlation times is consistent with the interpretation of reflection-generated inward-propagating fluctuations discussed in Section 3.4.

4. Discussion

In this paper, the properties of solar wind turbulence were measured in situ down to a heliocentric distance of 0.17 au for the first time. While many of the measured properties are shared with measurements nearer 1 au, significant differences include increased power levels (by more than two orders of magnitude in magnetic fluctuations and one order of magnitude in total energy), a $-3/2$ spectral index in all fields, a significantly smaller compressive component of the turbulence, a much smaller outer scale at which the nonlinear time is less than the travel time from the Sun, and an increase in the turbulence imbalance (measured through the cross-helicity σ_c or Elsasser ratio r_E) that is consistent with the generation of the inward-propagating component by reflection. The energy (enthalpy) flux in the turbulence increases to a significant fraction of the bulk solar wind kinetic energy flux in a manner consistent with models in which the solar wind is driven by this flux.

The Alfvénic turbulence spectra presented here were measured closer to the Sun and at higher frequencies than has previously been possible, e.g., with *Helios* (Tu & Marsch 1995; Bruno & Carbone 2013). The spectra at 0.17 au (Figures 1–3) have inertial range spectral indices of $\alpha \approx -3/2$ for both inward- and outward-propagating fluctuations. These spectra are similar to, although a little flatter than, the spectra predicted by Lithwick et al. (2007), whose model relies upon assumptions that may also describe reflection-driven turbulence in the solar wind (see Chandran & Perez 2019 for a more detailed discussion of this point). The reason why the observed spectra are flatter than the $-5/3$ spectra predicted by Lithwick et al. (2007) might be the presence of scale-dependent dynamic alignment (Boldyrev 2006) or intermittency (Chandran et al. 2015; Mallet & Schekochihin 2017), both of which progressively weaken the nonlinearity in a critically balanced cascade. The $\alpha \approx -3/2$ spectra are also consistent with some models of homogeneous imbalanced MHD turbulence that do not invoke wave reflection (Perez & Boldyrev 2009; Podesta & Borovsky 2010). Another possibility for the spectral index trend in Figure 2 is the turbulence transitioning from a much shallower spectrum closer to the Sun, e.g., the reflection-driven cascade model of Velli et al. (1989), which predicts a k^{-1} spectrum. A further possibility is that at smaller r , there is a more significant effect of the driving, which may affect the spectrum in different ways. First, the properties of the turbulent cascade may differ depending on whether it is forced at large scales or decaying; Chen et al. (2011) found that in a simulation of Alfvénic turbulence, the spectral indices of all fields vary from $-3/2$ to $-5/3$ as the simulation transitions from a forced to a decaying state. Second, closer to the Sun, there may be a stronger signature of the driving itself throughout the spectrum (as discussed later in this section). Future orbits of *PSP* at smaller

r will hopefully allow these various possibilities to be distinguished.

The decrease in magnetic compressibility closer to the Sun was shown to be associated with both a decrease in β and a reduction in the kinetic energy in the slow-mode component of the turbulence (Figure 5). One possible reason for the slow-mode component increasing as the solar wind travels from the Sun is continual local driving, e.g., from velocity shears (Roberts et al. 1992) or parametric decay (Del Zanna et al. 2001; Tenerani & Velli 2013; Bowen et al. 2018a). However, it is also possible that another process is acting to suppress the fluctuations in $|\mathbf{B}|$ nearer to the Sun. It has been proposed that a higher-order effect of large-amplitude Alfvén waves is to reduce the variations in $|\mathbf{B}|$, which can be thought of as an effect of the magnetic pressure force (Cohen & Kulsrud 1974; Vasquez & Hollweg 1996), similarly to the effect of the pressure anisotropy force at high β found recently (Squire et al. 2019). Future work could include further investigation of these possibilities and the nature of the compressive component.

The increase of the outer scale with r , approximately as $\propto r^{1.1}$, is qualitatively consistent with previous studies at larger distances. Specifically, the variation is consistent with previous results for the $1/f$ break evolution between 1.5 and 5 au in polar fast wind (Horbury et al. 1996) although shallower than the variation found in ecliptic fast wind from 0.3 to 5 au (Bruno & Carbone 2013) and steeper than found for the radial variation of the correlation scale from 0.3 to 5 au (Ruiz et al. 2014). The finding of the nonlinear time at the break scale being much less than the travel time from the Sun would indicate that the fluctuations in the flat scaling range (larger than the break scale) have had significant time for nonlinear processing, raising the question of why the break is not at lower frequencies. Possibilities for this include a nonlinear cascade that produces a $1/f$ spectrum (Velli et al. 1989; Verdini et al. 2012; Perez & Chandran 2013; Chandran 2018) or that the fluctuations in this range have reached a saturated state and cannot grow to larger amplitudes (Villante 1980; Matteini et al. 2018). The radial variation of the outer scale is the same (to within errors) as that of the ion break scale (Duan et al. 2020), indicating that the width of the MHD inertial range, ~ 3 decades, stays approximately constant from 0.17 to 1 au. This has important implications, e.g., the level of anisotropy at kinetic scales is determined by the extent of the inertial range (Goldreich & Sridhar 1995), and the possible heating mechanisms there depend on the level of anisotropy (Schekochihin et al. 2009).

The increase of energy flux in the fluctuations near the Sun, compared to the bulk solar wind kinetic energy flux, was found to be consistent with solutions of the turbulence-driven solar wind model of Chandran et al. (2011) down to 0.17 au. The enthalpy flux in the outward-propagating fluctuations (δz^+) was found to be $\sim 10\%$ of that in the bulk kinetic energy at this distance and $\sim 40\%$ if extrapolated to the Alfvén point, indicating a significant turbulence flux is likely within the corona. This increase of Alfvénic flux toward the Sun is also consistent with remote observations of Alfvén waves in the chromosphere and corona, which were measured to contain sufficient energy to accelerate the fast solar wind (De Pontieu et al. 2007; McIntosh et al. 2011). The *PSP* results indicate that turbulence-driven models (e.g., Cranmer et al. 2007; Chandran & Hollweg 2009; Verdini et al. 2009; Chandran et al. 2011;

van der Holst et al. 2014) remain a viable explanation for the acceleration of the solar wind from open field regions.

The radial variation of the inward-propagating component (δz^-) was also found to be consistent with the reflection-driven model of Chandran et al. (2011), which makes the reflection of the outward-propagating fluctuations (from the large-scale gradient in v_A) forming the inward ones a viable explanation for the decrease in imbalance at larger distances (Figures 4 and 7). This trend is qualitatively consistent with previous measurements at larger radial distances (Roberts et al. 1987; Tu & Marsch 1995; Bavassano et al. 1998, 2000; Matthaeus et al. 2004; Breech et al. 2005). However, it is possible that other mechanisms, such as local driving (Roberts et al. 1992; Matthaeus et al. 2004; Breech et al. 2005) and parametric decay (Marsch & Tu 1993; Del Zanna et al. 2001; Tenerani & Velli 2013; Bowen et al. 2018a) may also contribute, and future observations will be needed to distinguish these possibilities.

One relevant question is the relation between the turbulence and the large-amplitude fluctuations known as “switchbacks,” “jets,” or “spikes,” which appear more prominent closer to the Sun (Bale et al. 2019; Dudok de Wit et al. 2020; Horbury et al. 2020; Kasper et al. 2020; McManus et al. 2020). These are Alfvénic fluctuations which significantly change the magnetic field direction and appear to occur in patches (Horbury et al. 2020) with quiet periods in between (Bale et al. 2019) and are correlated and have a scale-invariant distribution (Dudok de Wit et al. 2020). The origin and role of these structures is an open question, in particular whether they are generated by the turbulence, are not initially but then become part of the cascade, or are unrelated altogether. Initial analysis indicates that while the amplitude of the fluctuations is lower in the quiet periods (Bale et al. 2019) and various kinetic waves become detectable (Bowen et al. 2020; Malaspina et al. 2020), in the inertial range both types of wind have a $-3/2$ spectrum consistent with turbulence, although the extent of this might be smaller in the quiet periods (Dudok de Wit et al. 2020). One possible interpretation is that these large-amplitude fluctuations represent the remnant of driving processes at the Sun that become part of the turbulent cascade as the solar wind expands. In this paper, all fluctuations are considered part of the turbulence cascade, although future work could investigate this relationship further.

With future *PSP* orbits, it will be possible to see how the trends measured in this paper continue to smaller distances to provide more insight into the fundamental nature of the cascade, directly measure the turbulence energy flux within the solar corona to determine its contribution to solar wind acceleration, examine the turbulence (Alexandrova et al. 2013; Chen 2016; Chen & Boldyrev 2017; Duan et al. 2020) and field-particle interactions (Chen et al. 2019) at kinetic scales to understand how it heats the corona and inner solar wind, and perhaps probe the nature of the turbulence-driving mechanisms. Such data, closer to the Sun and within the Alfvén point, promise to continue revealing more about the nature of plasma turbulence and the role it plays in the near-Sun environment.

C.H.K.C. is supported by STFC Ernest Rutherford Fellowship ST/N003748/2. S.D.B. acknowledges the support of the Leverhulme Trust Visiting Professorship program. D.B. is supported by STFC grant ST/P000622/1. B.D.G.C. is supported in part by NASA grants NNX17AI18G and 80NSSC19K0829. K.G.K. is supported by NASA ECIP grant

80NSSC19K0912. The *FIELDS* and *SWEAP* instrument teams are supported by NASA contract NNN06AA01C. We thank the members of the *FIELDS/SWEAP* teams and *PSP* community for helpful discussions. *PSP* data are available at the *SPDF* (<https://spdf.gsfc.nasa.gov>).

ORCID iDs

C. H. K. Chen  <https://orcid.org/0000-0003-4529-3620>
 S. D. Bale  <https://orcid.org/0000-0002-1989-3596>
 J. W. Bonnell  <https://orcid.org/0000-0002-0675-7907>
 D. Borovikov  <https://orcid.org/0000-0002-0151-7437>
 T. A. Bowen  <https://orcid.org/0000-0002-4625-3332>
 D. Burgess  <https://orcid.org/0000-0002-8175-9056>
 A. W. Case  <https://orcid.org/0000-0002-3520-4041>
 B. D. G. Chandran  <https://orcid.org/0000-0003-4177-3328>
 T. Dudok de Wit  <https://orcid.org/0000-0002-4401-0943>
 K. Goetz  <https://orcid.org/0000-0003-0420-3633>
 P. R. Harvey  <https://orcid.org/0000-0002-6938-0166>
 J. C. Kasper  <https://orcid.org/0000-0002-7077-930X>
 K. G. Klein  <https://orcid.org/0000-0001-6038-1923>
 K. E. Korreck  <https://orcid.org/0000-0001-6095-2490>
 D. Larson  <https://orcid.org/0000-0001-5030-6030>
 R. Livi  <https://orcid.org/0000-0002-0396-0547>
 R. J. MacDowall  <https://orcid.org/0000-0003-3112-4201>
 D. M. Malaspina  <https://orcid.org/0000-0003-1191-1558>
 A. Mallet  <https://orcid.org/0000-0001-9202-1340>
 M. D. McManus  <https://orcid.org/0000-0001-6077-4145>
 M. Moncuquet  <https://orcid.org/0000-0002-9621-0365>
 M. Pulupa  <https://orcid.org/0000-0002-1573-7457>
 M. L. Stevens  <https://orcid.org/0000-0002-7728-0085>
 P. Whittlesey  <https://orcid.org/0000-0002-7287-5098>

References

- Alazraki, G., & Couturier, P. 1971, *A&A*, **13**, 380
 Alexandrova, O., Chen, C. H. K., Sorriso-Valvo, L., Horbury, T. S., & Bale, S. D. 2013, *SSRv*, **178**, 101
 Badman, S., Bale, S. D., Martinez Oliveros, J. C., et al. 2020, *ApJS*, doi:10.3847/1538-4365/ab4a7
 Bale, S. D., Badman, S. T., Bonnell, J. W., et al. 2019, *Natur*, 576, 237
 Bale, S. D., Goetz, K., Harvey, P. R., et al. 2016, *SSRv*, **204**, 49
 Barnes, A. 1992, *RvGeo*, **30**, 43
 Bavassano, B., Dobrowolny, M., Mariani, F., & Ness, N. F. 1982, *JGR*, **87**, 3617
 Bavassano, B., Pietropaolo, E., & Bruno, R. 1998, *JGR*, **103**, 6521
 Bavassano, B., Pietropaolo, E., & Bruno, R. 2000, *JGR*, **105**, 15959
 Belcher, J. W. 1971, *ApJ*, **168**, 509
 Belcher, J. W., & Burchsted, R. 1974, *JGR*, **79**, 4765
 Belcher, J. W., & Davis, L. 1971, *JGR*, **76**, 3534
 Beresnyak, A., & Lazarian, A. 2008, *ApJ*, **682**, 1070
 Boldyrev, S. 2006, *PhRvL*, **96**, 115002
 Bourouaine, S., & Perez, J. C. 2018, *ApJL*, **858**, L20
 Bourouaine, S., & Perez, J. C. 2019, *ApJL*, **879**, L16
 Bowen, T. A., Badman, S., Hellinger, P., & Bale, S. D. 2018a, *ApJL*, **854**, L33
 Bowen, T. A., Mallet, A., Bonnell, J. W., & Bale, S. D. 2018b, *ApJ*, **865**, 45
 Bowen, T. A., Mallet, A., Huang, J., et al. 2020, *ApJS*, doi:10.3847/1538-4365/ab6c65
 Breech, B., Matthaeus, W. H., Minnie, J., et al. 2005, *GeoRL*, **32**, L06103
 Bruno, R. 2006, *SSRv*, **112**, 321
 Bruno, R., Bavassano, B., & Villante, U. 1985, *JGR*, **90**, 4373
 Bruno, R., & Carbone, V. 2013, *LRSF*, **10**, 2
 Case, A. W., Kasper, J. C., Stevens, M. L., et al. 2020, *ApJS*, doi:10.3847/1538-4365/ab5a7b
 Chandran, B. D. G. 2018, *JPIPh*, **84**, 905840106
 Chandran, B. D. G., Dennis, T. J., Quataert, E., & Bale, S. D. 2011, *ApJ*, **743**, 197
 Chandran, B. D. G., & Hollweg, J. V. 2009, *ApJ*, **707**, 1659
 Chandran, B. D. G., & Perez, J. C. 2019, *JPIPh*, **85**, 905850409

- Chandran, B. D. G., Schekochihin, A. A., & Mallet, A. 2015, *ApJ*, **807**, 39
- Chaston, C., Bonnell, J. W., Bale, S. D., et al. 2020, *ApJS*, submitted
- Chen, C. H. K. 2016, *JPIPh*, **82**, 535820602
- Chen, C. H. K., Bale, S. D., Salem, C. S., & Maruca, B. A. 2013, *ApJ*, **770**, 125
- Chen, C. H. K., & Boldyrev, S. 2017, *ApJ*, **842**, 122
- Chen, C. H. K., Klein, K. G., & Howes, G. G. 2019, *NatCo*, **10**, 740
- Chen, C. H. K., Mallet, A., Schekochihin, A. A., et al. 2012, *ApJ*, **758**, 120
- Chen, C. H. K., Mallet, A., Yousef, T. A., Schekochihin, A. A., & Horbury, T. S. 2011, *MNRAS*, **415**, 3219
- Cohen, R. H., & Kulsrud, R. M. 1974, *PhFI*, **17**, 2215
- Coleman, P. J. 1968, *ApJ*, **153**, 371
- Cranmer, S. R., Asgari-Targhi, M., Miralles, M. P., et al. 2015, *RSPTA*, **373**, 20140148
- Cranmer, S. R., Matthaeus, W. H., Breech, B. A., & Kasper, J. C. 2009, *ApJ*, **702**, 1604
- Cranmer, S. R., & van Ballegoijen, A. A. 2005, *ApJS*, **156**, 265
- Cranmer, S. R., van Ballegoijen, A. A., & Edgar, R. J. 2007, *ApJS*, **171**, 520
- De Pontieu, B., McIntosh, S. W., Carlsson, M., et al. 2007, *Sci*, **318**, 1574
- Del Zanna, L., Velli, M., & Londrillo, P. 2001, *A&A*, **367**, 705
- Dmitruk, P., Matthaeus, W. H., Milano, L. J., et al. 2002, *ApJ*, **575**, 571
- Duan, D., Bowen, T. A., Chen, C. H. K., et al. 2020, *ApJS*, doi:10.3847/1538-4365/ab672d
- Dudok de Wit, T., Krasnoselskikh, V. V., Bale, S. D., et al. 2020, *ApJS*, doi:10.3847/1538-4365/ab5853
- Elsasser, W. M. 1950, *PhRv*, **79**, 183
- Fox, N. J., Velli, M. C., Bale, S. D., et al. 2016, *SSRv*, **204**, 7
- Fratemale, F., Pogorelov, N. V., Richardson, J. D., & Tordella, D. 2019, *ApJ*, **872**, 40
- Freeman, J. W. 1988, *GeoRL*, **15**, 88
- Gazis, P. R., & Lazarus, A. J. 1982, *GeoRL*, **9**, 431
- Goldreich, P., & Sridhar, S. 1995, *ApJ*, **438**, 763
- Hansteen, V. H., & Velli, M. 2012, *SSRv*, **172**, 89
- Heinemann, M., & Olbert, S. 1980, *JGR*, **85**, 1311
- Hellinger, P., Matteini, L., Štverák, Š., Trávníček, P. M., & Marsch, E. 2011, *JGR*, **116**, A09105
- Hollweg, J. V. 2008, *JApA*, **29**, 217
- Horbury, T., Woolley, T., Laker, R., et al. 2020, *ApJS*, doi:10.3847/1538-4365/ab5b15
- Horbury, T. S., & Balogh, A. 2001, *JGR*, **106**, 15929
- Horbury, T. S., Balogh, A., Forsyth, R. J., & Smith, E. J. 1996, *A&A*, **316**, 333
- Horbury, T. S., Forman, M., & Oughton, S. 2008, *PhRvL*, **101**, 175005
- Horbury, T. S., Forman, M. A., & Oughton, S. 2005, *PPCF*, **47**, B703
- Howes, G. G., Bale, S. D., Klein, K. G., et al. 2012, *ApJL*, **753**, L19
- Iroshnikov, P. S. 1963, *AZh*, **40**, 742
- Isaacs, J. J., Tessein, J. A., & Matthaeus, W. H. 2015, *JGR*, **120**, 868
- Kasper, J., Bale, S. D., & Belcher, J. W. 2020, *Natur*, **576**, 228
- Kasper, J. C., Abiad, R., Austin, G., et al. 2016, *SSRv*, **204**, 131
- Kiyani, K. H., Osman, K. T., & Chapman, S. C. 2015, *RSPTA*, **373**, 20140155
- Klein, K. G., Howes, G. G., TenBarge, J. M., et al. 2012, *ApJ*, **755**, 159
- Klein, K. G., Perez, J. C., Verscharen, D., Mallet, A., & Chandran, B. D. G. 2015, *ApJL*, **801**, L18
- Kraichnan, R. H. 1965, *PhFI*, **8**, 1385
- Krishna Jagarlamudi, V., Dudok de Wit, T., Krasnoselskikh, V., & Maksimovic, M. 2019, *ApJ*, **871**, 68
- Leer, E., Holzer, T. E., & Fla, T. 1982, *SSRv*, **33**, 161
- Lithwick, Y., Goldreich, P., & Sridhar, S. 2007, *ApJ*, **655**, 269
- Malaspina, D. M., Halekas, J., Bercic, L., et al. 2020, *ApJS*, doi:10.3847/1538-4365/ab4c3b
- Mallet, A., & Schekochihin, A. A. 2017, *MNRAS*, **466**, 3918
- Marsch, E., Schwenn, R., Rosenbauer, H., et al. 1982, *JGR*, **87**, 52
- Marsch, E., & Tu, C.-Y. 1993, *JGR*, **98**, 21
- Matteini, L., Stansby, D., Horbury, T. S., & Chen, C. H. K. 2018, *ApJL*, **869**, L32
- Matthaeus, W. H., & Goldstein, M. L. 1982, *JGR*, **87**, 10347
- Matthaeus, W. H., & Goldstein, M. L. 1986, *PhRvL*, **57**, 495
- Matthaeus, W. H., Minnie, J., Breech, B., et al. 2004, *GeoRL*, **31**, 12803
- Matthaeus, W. H., Zank, G. P., Oughton, S., Mullan, D. J., & Dmitruk, P. 1999a, *ApJL*, **523**, L93
- Matthaeus, W. H., Zank, G. P., Smith, C. W., & Oughton, S. 1999b, *PhRvL*, **82**, 3444
- McIntosh, S. W., de Pontieu, B., Carlsson, M., et al. 2011, *Natur*, **475**, 477
- McManus, M., Bowen, T. A., Mallet, A., et al. 2020, *ApJS*, doi:10.3847/1538-4365/ab6dce
- Mihalov, J. D., & Wolfe, J. H. 1978, *SoPh*, **60**, 399
- Moncuquet, M., Meyer-Vernet, N., Issautier, K., et al. 2020, *ApJS*, doi:10.3847/1538-4365/ab5a84
- Monin, A. S., & Yaglom, A. M. 1975, *Statistical Fluid Mechanics 2* (Cambridge, MA: MIT Press)
- Parashar, T., Golstein, M. L., Maruca, B., et al. 2020, *ApJS*, doi:10.3847/1538-4365/ab64e6
- Parker, E. N. 1958, *ApJ*, **128**, 664
- Parker, E. N. 1965, *SSRv*, **4**, 666
- Perez, J. C., & Boldyrev, S. 2009, *PhRvL*, **102**, 025003
- Perez, J. C., & Chandran, B. D. G. 2013, *ApJ*, **776**, 124
- Podesta, J. J., & Bhattacharjee, A. 2010, *ApJ*, **718**, 1151
- Podesta, J. J., & Borovsky, J. E. 2010, *PhPI*, **17**, 112905
- Richardson, J. D., Paularena, K. I., Lazarus, A. J., & Belcher, J. W. 1995, *GeoRL*, **22**, 325
- Roberts, D. A. 2010, *JGR*, **115**, 12101
- Roberts, D. A., Goldstein, M. L., Matthaeus, W. H., & Ghosh, S. 1992, *JGR*, **97**, 17115
- Roberts, D. A., Klein, L. W., Goldstein, M. L., & Matthaeus, W. H. 1987, *JGR*, **92**, 11021
- Ruiz, M. E., Dasso, S., Matthaeus, W. H., & Weygand, J. M. 2014, *SoPh*, **289**, 3917
- Schekochihin, A. A., Cowley, S. C., Dorland, W., et al. 2009, *ApJS*, **182**, 310
- Squire, J., Schekochihin, A. A., Quataert, E., & Kunz, M. W. 2019, *JPIPh*, **85**, 905850114
- Szabo, A., Larson, D., Whittlesey, P., et al. 2020, *ApJS*, doi:10.3847/1538-4365/ab5dac
- Taylor, G. I. 1938, *RSPSA*, **164**, 476
- Tenerani, A., & Velli, M. 2013, *JGR*, **118**, 7507
- Tu, C.-Y., & Marsch, E. 1995, *SSRv*, **73**, 1
- Usmanov, A. V., Matthaeus, W. H., Goldstein, M. L., & Chhiber, R. 2018, *ApJ*, **865**, 25
- van Ballegoijen, A. A., & Asgari-Targhi, M. 2017, *ApJ*, **835**, 10
- van der Holst, B., Sokolov, I. V., Meng, X., et al. 2014, *ApJ*, **782**, 81
- Vasquez, B. J., & Hollweg, J. V. 1996, *JGR*, **101**, 13527
- Vech, D., Kasper, J. C., Klein, K. G., et al. 2020, *ApJS*, doi:10.3847/1538-4365/ab60a2
- Velli, M. 1993, *A&A*, **270**, 304
- Velli, M., Grappin, R., & Mangeney, A. 1989, *PhRvL*, **63**, 1807
- Verdini, A., Grappin, R., Pinto, R., & Velli, M. 2012, *ApJL*, **750**, L33
- Verdini, A., & Velli, M. 2007, *ApJ*, **662**, 669
- Verdini, A., Velli, M., & Buchlin, E. 2009, *ApJL*, **700**, L39
- Verdini, A., Velli, M., Matthaeus, W. H., Oughton, S., & Dmitruk, P. 2010, *ApJL*, **708**, L116
- Verscharen, D., Chen, C. H. K., & Wicks, R. T. 2017, *ApJ*, **840**, 106
- Villante, U. 1980, *JGR*, **85**, 6869
- Wicks, R. T., Mallet, A., Horbury, T. S., et al. 2013, *PhRvL*, **110**, 025003